Understanding the use of carbon-based porous transport layers at the cathode in PEM water electrolysis

Niklas Hensle [a,b,*] , Justin Hoffmann [a], Zabihollah Najafianashrafi [c], Tom Smolinka [a],
Po-Ya Abel Chuang [c] , André Weber [b]

[a] *Fraunhofer Institute for Solar Energy System ISE, Heidenhofstr. 2, 79110, Freiburg, Germany*
[b] *Institute for Applied Materials (IAM-ET), Karlsruhe Institute of Technology (KIT), Adenauerring 20b, 76131, Karlsruhe, Germany*
[c] *Thermal and Electrochemical Energy Laboratory (TEEL), University of California, Merced, 5200 North Lake Rd, Merced, CA95343, USA*

HIGHLIGHTS

- Gas diffusion layer (GDL) compression significantly influences cell performance.
- Bipolar plates require proper coating when being compressed against GDLs.
- Micro porous layer at the cathode is crucial for low loading catalyst layers.
- PTFE additives of 5 wt% do not improve performance but increase ohmic resistance.

ABSTRACT

Cost reduction of cell components is a major issue in PEM water electrolysis. For the anode, titanium materials with noble metal coatings represent the state of the art. For the cathode, the use of carbon-based porous transport layers, also known as gas diffusion layers (GDLs), is gaining prominence due to their significantly lower costs compared to titanium-based materials. In PEM fuel cells, carbon-based GDLs are well-established, with advancements in contact and gas/water transport achieved through micro porous layers and hydrophobic treatments. In contrast, in PEM water electrolysis, topics like interfacial contact, compression behavior, and the use of additives for carbon-based GDLs have not been widely discussed in the literature yet. With this work, we present a fundamental performance investigation of these aspects. We investigate cell performance using voltage breakdown analysis and electrochemical impedance spectroscopy, combined with subsequent Distribution of Relaxation Time analysis. Our findings highlight the effect of GDL compression and underscore the necessity of coated flow fields at the cathode. PTFE additives were found to have minimal influence on cell behavior, regardless of the presence or absence of water flow at the cathode. However, the use of micro porous layers demonstrated positive effects, particularly for ultra-low cathode catalyst loadings.

1. Introduction

For cost reduction, carbon-based porous transport layers (PTLs), which are often also referred to as gas diffusion layers (GDLs) since the components originate from the development of fuel cells, are an attractive option for use on the cathode side of a PEM water electrolysis cell. Compared to coated titanium-based PTLs, carbon-based materials offer significantly lower material and preparation costs [1,2]. On the anode side, a high oxygen partial pressure and overpotentials exceeding 1.5 V are expected. Therefore, carbon-based materials are not stable for long-term operation due to corrosion issues [3,4]. In contrast, the reducing hydrogen atmosphere and low overpotentials at the cathode make carbon-based GDLs a viable option.

In proton exchange membrane fuel cells (PEMFC), carbon-based GDLs have been extensively investigated over the past 30 years. Studies on interfacial contact [5,6], compression behavior [7–9], and hydrophobic treatments [10,11] have been published. Today, carbon-based GDLs are standard in all PEMFC stacks. Furthermore, it is state-of-the-art to use a micro porous layer (MPL) between the GDL and the catalyst layer to ensure intimate contact and provide gas and water transport paths [12,13]. Such GDL materials, optimized for PEMFC applications, are often used in PEM water electrolysis without a detailed examination of their advantages or disadvantages [14–21]. There are only a few investigations on the carbon-based material and its influence on cell behavior.

Ortiz et al. analyzed a PEM water electrolysis cell, varying the cell compression between 20 % and 60 % and discussed the influence on membrane deformation and the cell performance [22]. They observed a

---

decreasing high frequency resistance (HFR) of around 15 m$\Omega \cdot$ cm^2 but constant kinetic behavior when increasing the compression. At 60 % increasing residual overpotentials are detected which are attributed to increasing mass transport resistance. The optimal compression was found to be at 40 %, where the performance peaks; slightly lower compression does not show significantly worse performance but may be more stable due to less membrane deformation.

Staehler et al. investigated the hydrogen permeation through the membrane depending on the cell compression [23]. They used a range of compression between 12.75 % and 45 % and detected decreasing HFR with increasing compression which is interpreted as increased contact pressure on the electrode. However, increased compression leads to higher values of the HFR-free polarization curve towards high current densities which is referred to increasing mass transport resistance. Furthermore, they found that the correlation between hydrogen permeation current and electrical cell current is non-linear and highly dependent on the cell compression.

Martin et al. analyzed hydrogen permeation and cell performance at cell compression and cathode gas pressure variations [24]. With a GDL compression between 5 % and 42.5 %, they observed decreasing HFR with increasing compression and increasing mass transport overpotentials, which is in great accordance with the studies mentioned above.

Kang et al. investigated the influence of PTFE (Polytetrafluoroethylene) as additives in conventional GDL material implemented at the anode of a PEM water electrolysis cell [25], which is rather untypical since carbon-based material is not stable for long-term operation at the anode. However, to explain the influence on overpotentials with a focus on the two-phase flow, this is a valid approach. They observed an increase in diffusion-related resistance of >10 mΩ cm^2 when adding 5 wt % PTFE to the GDL, indicating that a hydrophobic treatment leads to inhibited water transport.

To gain a better understanding of carbon-based GDLs in PEM water electrolysis cells, we present fundamental investigations into the effects of varying GDL compression on cell performance. Using confocal laser scanning microscopy (CLSM) and ex situ compression analysis, we provide detailed insights into compression behavior. The contact resistance between gold-coated and uncoated titanium-based flow fields compressed against carbon-based GDLs and titanium-based PTLs is analyzed during the electrochemical characterization of single cells. Furthermore, we examine the influence of hydrophobic treatment and MPLs. As the membrane-electrode assembly, we use a commercial catalyst-coated membrane (CCM) with state-of-the-art catalyst loading and a purpose-made CCM with low cathode catalyst loading produced at Fraunhofer ISE.

With polarization curve measurements up to 5 A cm^{-2} and subsequent voltage breakdown analysis, we investigate the influence on ohmic, kinetic, and residual overpotentials. Furthermore, we examine polarization processes using electrochemical impedance spectroscopy (EIS) combined with subsequent Distribution of Relaxation Time (DRT) analysis.

Our findings demonstrate that cell compression plays a major role in cell performance. The coating of flow fields is critical when using carbon-based GDLs but appears to be less important when in contact with titanium-based PTLs. No substantial influence of PTFE additives in the cathode GDL was observed. The use of MPLs seems to be beneficial only when operating with low-loading cathode catalyst layers, which are of high interest for achieving PEM water electrolysis development goals. It is important to note that these results pertain only to cell performance and do not yet allow for any statements regarding durability.

2. Experimental

2.1. Conducted studies & cell materials

In this work, four aspects of the use of carbon-based GDL materials at the cathode in PEM water electrolysis cells are investigated and analyzed based on cell performance:

- Compression behavior of GDLs,
- Contact resistance of GDLs with coated and uncoated flow fields,
- Influence of micro porous layer (MPL) on GDLs,
- Hydrophobic treatment (PTFE impregnation) of GDLs.

The CCM used is a state-of-the-art, commercially available E400 Gen.3 by *Greenerity GmbH*, Germany, consisting of a membrane thickness of 125 µm (Nafion® N115) and Pt/C and IrOx catalyst layers. At the anode, a platinum-coated 250 µm titanium fiber porous transport layer (PTL) from *Bekaert SA,* Belgium (2GDL-10-0.25) is employed. The baseline material at the cathode is AvCarb MGL370 from *AvCarb Material Solutions,* USA, with a nominal uncompressed thickness of 370 µm.

For the MPL study, the GDL material was prepared by the University of California, Merced (UCM). A MPL layer was coated on the side of the GDL facing the catalyst layer. One sample has 5 wt% PTFE impregnation of the GDL, while the other without PTFE impregnation.

To evaluate the influence of the MPL on CCMs with low catalyst loading, an additional CCM was produced in-house at Fraunhofer ISE with reduced catalyst loading at the cathode. A Nafion®-based N115 membrane was coated with an anode loading of (1.88 ± 0.04) mg$_{Ir} \cdot$cm^{-2} using catalyst powder supplied by *Alfa Aesar*, USA, to achieve a state-of-the-art anode configuration. In contrast, the cathode was coated with only (0.054 ± 0.003) mg$_{Pt} \cdot$cm^{-2}, with catalyst provided by *Umicore AG & Co. KG*, Germany. Both catalyst layers were applied via screen printing onto a decal foil and later hot-pressed onto the membrane.

2.2. Test cell

The test cell used in this study was developed in-house by Fraunhofer ISE. It consists of two identical cell bodies made of titanium grade 2. Polymer frames made of PEEK (polyether ether ketone) are screwed onto the cell bodies. Flat sealings are set into the groove of the polymer frame to guarantee proper gas tightness. With different heights of the polymer frames the cell compression can be adjusted. In this study, the polymer frame at the anode remains constant and we assume no compression of the used titanium-based PTL. The polymer frame at the cathode is varied in height to achieve the different compressions intended; see section *Compression study and microscopy of GDL material*. The active area of the cell is 4 cm^2, with a straight parallel gold coated flow field design consisting of 10 channels each with a cross-sectional area of 1×1 mm^2. The nine lands in between the channels have a width of 0.9 mm. The cell has a compression system with the possibility to monitor the applied compression force during the measurements. With pressure paper analysis before each measurement the pressure distribution of the flat sealing and active area is analyzed. To measure the temperature either the water flow before and after the cell or an internal temperature sensor in the cell body right underneath the flow field at anode and cathode can be used. A more detailed description of the cell is provided in Ref. [26].

2.3. Test bench

An in-house developed test bench at Fraunhofer ISE was used to conduct the electrochemical measurements. The water flows at the anode and cathode can be controlled independently. Filters and ion exchangers with water conductivity measurements are implemented to guarantee high water quality of $\langle 0.1 \; \mu S \cdot cm^{-1}$. With flow heaters implemented in the half-cell water loops, the water temperature can be set for anode and cathode independently and controlled before, after, or internally within the test cell. Although this study is only conducted at ambient pressure, the test bench can operate at up to 50 bar differential and balanced pressure. An electrochemical workstation by *Zahner-Elektrik GmbH & Co. KG*, Germany is used, consisting of *Zahner Zennium*

Pro and *Zahner PP242, which enables measurements up to 40 A*. The test bench is automated using in-house produced test bench software based on LabVIEW and Python.

2.4. Compression study and microscopy of GDL material

The polymer frame screwed onto the test cell body features a so-called hard stop that prevents further compression. The nominal compression K_{nom} is defined as the planned compression of the GDL due to the height of the hard stop (h_{hs}) compared to the height of the pristine GDL (h_{GDL}) and given by the following Equation:

$$K_{\mathrm{nom}} = \frac{h_{\mathrm{GDL}} - h_{hs}}{h_{\mathrm{GDL}}} \bullet 100\% \tag{1}$$

A schematic diagram is provided in the Supplementary Information SI 1. Polymer frames with different hard stop heights were used to achieve 0 %, 10 %, 20 %, 40 %, 60 % and 80 % compression. To determine the necessary clamping force for the hard stop to be reached, pressure distribution measurements were performed, using pressure paper by *FUJIFILM*, Japan. Once the pressure on the hard stop exceeds 2.5 MPa over the entire hard stop area, the cell is considered to be fully and homogeneously compressed. A similar approach to achieving nominal compression was also employed in Ref. [24].

To validate that actual compression matches the nominal compression, compressed GDLs were analyzed using CLSM after pressure distribution measurements (to confirm the good manufacturing quality of the polymer frame) and after electrochemical characterization.

A microscope by *Olympus* (*LEXT OLS5100*), Japan with a 405 nm diode laser and MPLAPON20xLEXT (0.6 N A.) objective was used. Image processing and evaluation were conducted using the software provided by Olympus (Analysis Application Version 3.1.1.296). The compression of the GDL is measured by the height difference between compressed (area over flow field lands) and uncompressed (area over flow field channels) carbon fibers on the surface of the sample. The fibers considered for the compression measurement are manually selected. This involves taking a grid of 17 × 17 images with a 10 % overlap, stitched together to achieve high precision in the x and y axes, covering an area of approximately 1 × 1 cm^2 at the central part of the GDL. A z-stack of images is captured at each image position with a step size of 1.2 μm, starting at the lowest focus point. The topography is determined by analyzing the variations in the intensity signal of the laser at different focal planes. For post-mortem characterization, samples were dried overnight to remove water content that could affect the measurement data. An example of a compression measurement is presented in the Supplementary Information SI 2. All further images of PTFE and MPL presented in this work were also recorded using this microscope.

2.5. Ex situ compression analysis

To investigate the mechanical properties of the carbon-based GDL, ex situ compression tests were conducted using a custom-built setup for micromechanical testing by *Fraunhofer IWM*. The setup is based on the work of Kennerknecht [27] and Straub [28]. For further information on the setup, we refer to *Fraunhofer* IWM. Similar micromechanical testing setups were utilized in Refs. [29,30].

To simulate compression of the cell setup used in this work, a custom-built sample holder and punch with five channels, identical to the land-channel structure of the flow field, are used together with the GDL, CCM, and PTL. A piezo actuator, with a step size of 1.8 nm and a speed of 1 μm s^{-1}, initially moves to the zero position. The sample is compressed in 5 % compression steps until the maximum force of 100 N is reached. Each compression step is followed by a relaxation phase of 30 s to allow the system to stabilize. During the test, imaging through a microscope captured the deformation and intrusion of the GDL into the channel. These images, along with continuous measurements of force and displacement, ensured detailed monitoring throughout the experiment. Displacement data and force at the end of relaxation phases are converted into compression and clamping pressure, respectively. Graphical analysis of the images determines the GDL intrusion. Measurements were conducted at room temperature and under dry conditions. To demonstrate reproducibility, the measurements were performed twice. For the analysis of channel intrusion, compression, and clamping pressure, mean values with error bars from both measurements are shown.

2.6. Electrochemical characterization

For the analysis of cell performance, polarization curves between 0.01 A cm^{-2} and 5 A cm^{-2} at 80 °C and 60 °C were conducted with a flow rate at the anode of 150 ml min^{-1} and ambient pressure. The cathode is typically not supplied with water; however, for some measurements, a water flow of 150 ml min^{-1} is also applied to the cathode. Each current step of the polarization curve was held for 300 s, and in the last 30 s, the high-frequency resistance (HFR) was measured by recording an impedance spectrum between 100 kHz and 1000 Hz and analyzing the impedance at a 0° phase angle. At selected current density steps, electrochemical impedance spectroscopy (EIS) was performed between 100 kHz and 100 mHz with 10 measurement points per decade and a 10-period integration time.

Before characterization, the dry assembled cell is compressed with a 1 kN force, and water at 80 °C is flushed at the anode for 1 h. After this, the target compression force is applied, and two galvanostatic steps of 0.2 A cm^{-2} and 1 A cm^{-2} for 30 min each are conducted; afterwards, a voltage of 1.7 V is held for 12 h. For the low-loading CCM produced by Fraunhofer ISE, the cell is conditioned with polarization curve measurements in the same current density range as the latter characterization, repeated 5 times. Subsequently, a constant voltage of 1.9 V is held for 5 h, followed by 10 h at 2.1 V.

All electrochemical measurements are performed twice to ensure reproducibility. For the voltage breakdown analysis, the mean value with error bars from both measurements is shown. For the EIS, the results of one of the measurements are presented.

2.7. Performance and impedance analysis

To investigate the cell performance, the cell voltage is separated into its ohmic (η_{Ω}), kinetic (η_{kin}) and residual overpotentials (η_{res}), in addition the thermodynamic cell voltage $U_0(p,T)$, see Equation (2).

$$U_{\mathrm{cell}} = U_0(p,T) + \eta_{\Omega} + \eta_{\mathrm{kin}} + \eta_{\mathrm{res}} \tag{2}$$

The pressure and temperature dependency of the thermodynamic cell voltage $U_0(p,T)$ is determined by Nernst Equation [31] and the approximations shown in Equations (3) and (4) [32,33].

$$U_0(T) = 2\,F\Delta G(T) = 1.5184 - 1.5421{\cdot}10^{-3}{\cdot}T + 9.523{\cdot}10^{-5}{\cdot}T{\cdot}\log(T) + 9.84{\cdot}10^{-8}{\cdot}T^2 \tag{3}$$

$$U_0(p,T) = U_0(T) + \frac{3R{\cdot}T}{4F}{\cdot}\log\,(p) \tag{4}$$

With the measurement of the HFR, the ohmic overpotentials (η_{Ω}) can be estimated, see Equation (5) and subtracted from the polarization curve measurements to analyze the ohmic-free cell behavior over the current density. The HFR is determined by the real part of the impedance at the intersection with Im(Z) = 0 at frequencies greater than 1 kHz. It should be noted, that this type of determination does not exclude high-frequency artefacts, as presented in Refs. [14,34].

$$\eta_{\Omega} = R_{\mathrm{HFR}}{\cdot}j \tag{5}$$

The kinetic overpotential (η_{kin}) is modeled by the Tafel approach, which includes kinetics of both the anode and cathode. We explicitly do

not assume the cathode to be non-polarizable, as we use low cathode loadings, see Fig. 7. The HFR-free polarization curve is fitted over a decadic logarithmic scale of the current density between 0.01 A cm^{-2} and 0.1 A cm^{-2} to determine the value of the Tafel slope b. With this value, η_{kin}, which depends on the current density, can be determined [35], see Equation (6).

$$\eta_{kin} = b \cdot \log \left(\frac{j}{1 \, A \cdot cm^{-2}} \right) \qquad (6)$$

All remaining overpotentials in this study are described as residual overpotentials η_{res}, which are often related to diffusive and convective mass transport processes [36,37]. In our previous work, we showed that, besides conventional (capacitive) mass transport contributions, a yet unknown process of inductive type needs to be considered at current densities greater than 1 A cm^{-2} [38,39] in impedance spectra which may also be included in η_{res}. The origin of the inductive loop is not yet clear, however, based on our findings we would relate it to a membrane and/or ionomer effect. In PEM fuel cells, both membrane and ionomer effects, as well as changes of the oxygen reduction reaction catalyst layer have been reported. Therefore, we would not neglect that the inductive loop is also related to the anodic catalyst layer properties and their change during operation.

Besides the inductive effect, other resistances are reported to be included in η_{res}, such as electronic and ionic in-plane catalyst layer resistance [40,41], which usually appear at higher frequencies as charge transfer resistance and are difficult to estimate due to high-frequency artefacts in impedance spectra.

With impedance-based analysis, the cell behavior can be deconvoluted by the time constants of the electrochemical processes. This allows for a more precise analysis of the electrochemical processes than merely deconvoluting the DC overpotentials of the cell polarization. Since high data quality is necessary to properly analyze impedance spectra, the Kramers Kronig test is carried out for each spectra shown in this work, with the requirement to fulfill residuals below ±1% [42,43]. Processes with similar time constants often show overlapping impedance data, which cannot be deconvoluted properly. Distribution of Relaxation Time (DRT) analysis provides more information about the polarization processes and their peak frequencies [44–47]. A DRT approach provided by KIT which alloes for the analysis of low-frequency inductive processes [48], is used in this work with a Tikhonov regularization parameter of $\lambda = 5 \cdot 10^{-3}$, as identified to be sufficient in our previous work [38].

2.8. PEM fuel cell testing

Fuel cell testing was performed using an automated G20 test station by *Greenlight Innovation*, Canada for precise control and data acquisition. Details of the test station as well as the break-in procedures can be found in our previous work [11]. Fuel cell performance data was collected under dry (70 °C, 64 % RH (relative humidity), 100 kPa) and wet (70 °C, 100 % RH, 300 kPa) conditions. Each voltage set point was stabilized for 10 min, and the data were averaged over the final minute to ensure steady-state operation. A Gamry Reference 3000 coupled with a 30k Booster was used to determine HFR. Ultrahigh purity gases (99.999 % H$_2$, air, and N$_2$) were supplied at flow rates of 0.40 NLPM (normal liter per minute) for the anode and 2.0 NLPM for the cathode.

2.9. PEM fuel cell components

The baseline GDL (AvCarb MGL370) was used in the fuel cell experiments. To study the effects of PTFE treatment and MPL, a modified GDL sample, referred to as UCM MPL + PTFE, was prepared. Detailed PTFE impregnation, MPL coating, and GDL sintering processes can also be found in Ref. [11]. The MPL, composed of 25 wt% PTFE and 75 wt% acetylene black carbon powder, was applied to the GDL with a target loading of 1.5 mg·cm^{-2}. MEAs from Ion Power, USA, Nafion 211

membrane with catalyst loading of 0.3 mg$_{Pt}$·cm^{-2} on both the anode and cathode sides, were used for the fuel cell testing. A straight-parallel channel flow field, machined from POCO graphite plates with high electrical and thermal conductivity, was employed in the fuel cell experiments. The flow field channels had dimensions of 660 μm in width, 800 μm in depth, and a 1:1 channel-to-land ratio [11].

3. Results & discussion

3.1. GDL compression behavior

The results of the post-mortem CLSM analysis of the GDL material and the ex situ compression analysis by *Fraunhofer IWM* are presented in Fig. 1. In Fig. 1 a) the results of the CLSM scans at 10 %, 20 %, 40 %, and 60 % nominal compression are shown, the extracted values for all compression analyses are listed in Table 1. The GDL compression is defined by the difference in height between the land and the channel areas, assuming that the GDL does not significantly change in height over the channel compared to the pristine GDL height. The lowest focus point was set within the pores of the compressed fibers, leading to negative values in the CLSM analysis. The top fiber layer of compressed fibers is established as reference level ($h = 0$ μm). Positive values extend up to the surface of the uncompressed fibers, indicating GDL compression.

The mean value and standard deviation were calculated from two different samples, which were dried after individual electrochemical characterization. The samples at 80 % compression were destroyed after the electrochemical characterization and could therefore not be analyzed with the microscope, indicating that an excessively high force was applied. The difference between nominal compression and post-mortem measured compression is in good agreement, indicating that the planned (nominal) compression was present during the electrochemical testing. It should be noted that the GDL sample may exhibit non-negligible elastic compression behavior. Since the microscopy analysis is conducted after the relaxation of the material, the compression during electrochemical characterization may have been even higher.

Fig. 1 b) shows the images taken during the compression analysis conducted at Fraunhofer IWM at the same compression steps as in Fig. 1 a). The compression is determined by the height change of the displacement sensor relative to the pristine GDL height. The starting point, which corresponds to 0 % compression, is determined by the force sensor at the first time point when a force greater than 0 N is measured. Since the GDL sample is slightly pressed forward during compression, the land height is obscured, which can lead to misinterpretations. Therefore, we marked the land height in the uncompressed condition (see the dashed line in red). The GDL material becomes more compressed over the flow field lands and is pressed into the flow field channels. A rearrangement of the fibers is observed as they break, which may significantly change the GDL properties and theoretically lead to better electrical bulk conductivity, smaller porosity, and a more uniform mean pore size distribution over the flow field lands. Based on the images shown, an influence on interfacial contact can be inferred when comparing the different compressions. To better understand the behavior during compression, a video of all compression steps can be found in the Supplementary Information SI 3.

Fig. 1 c) and 1 d) show the intrusion into the channel and the clamping pressure during the compression analysis at Fraunhofer IWM. The intrusion into the channel is analyzed by visually determining the height of the GDL over the channels compared to the land height, see the red dashed line in Fig. 1 b). The clamping pressure is determined by referencing the measured force to the area of the flow field lands. Each measurement was conducted twice; the error bars indicate reproducibility.

The changes in intrusion into the channel and clamping pressure
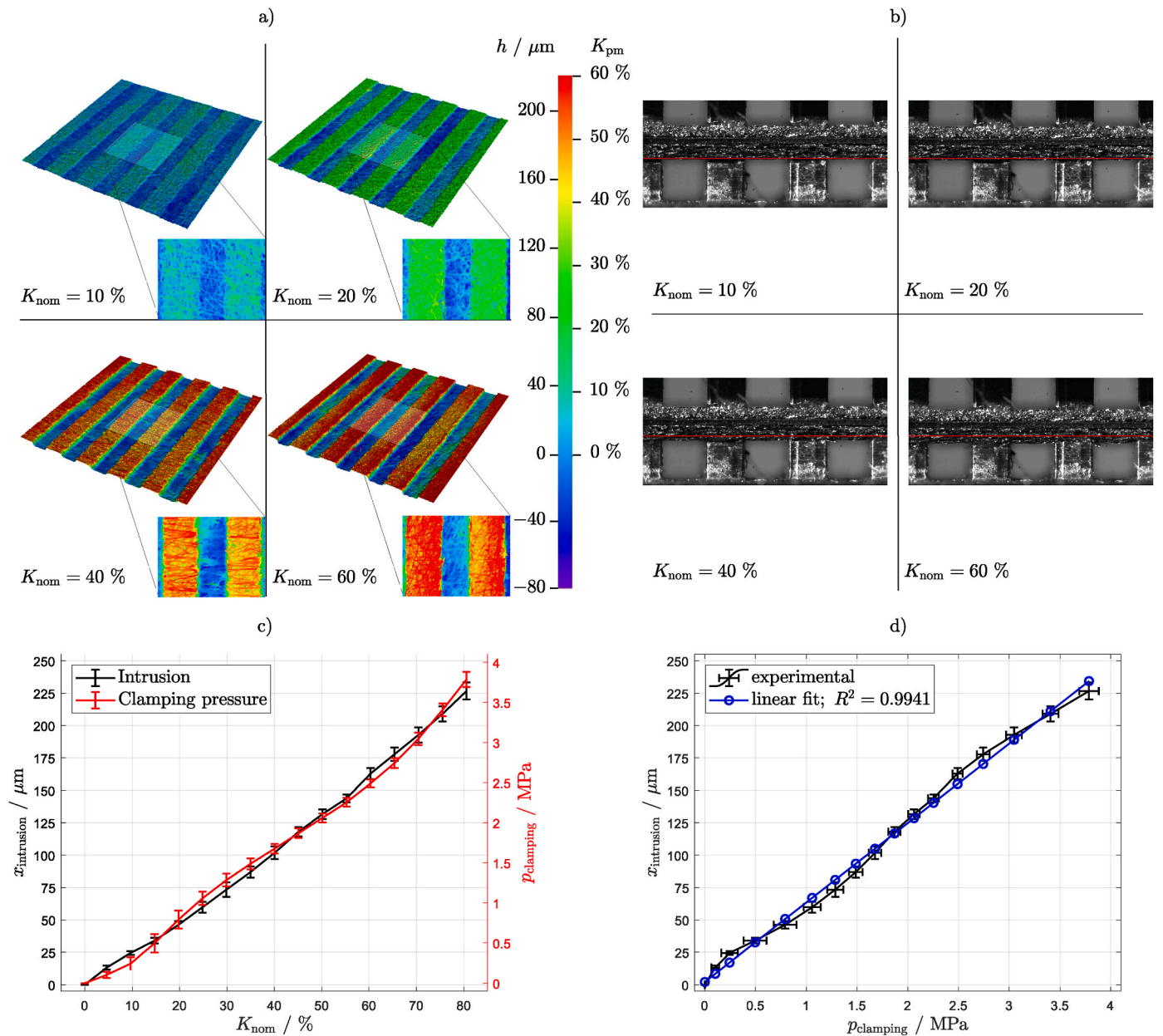
Fig. 1. Ex situ analysis of different compression of the GDL. a) post-mortem CLSM scans of the GDL. b) visualization of the compression analysis (whole video in SI 3 and c) analysis of the channel intrusion and clamping pressure over GDL compression at *Fraunhofer IWM*.

Table 1
Compression results of the post-mortem CLSM analysis.

$K_{nom}/$ %	$h_{GDL}/\mu m$	$K_{pm}/$%
0	14.0 ± 0.4	3.8 ± 0.1
10	35.7 ± 1.4	9.6 ± 0.4
20	72.2 ± 21.9	19.5 ± 5.9
40	170.9 ± 20.8	46.2 ± 5.6
60	221.2 ± 10.3	59.8 ± 2.8
80	Not evaluable	Not evaluable

both appear to increase with increasing compression, as shown by the non-linear behavior in Fig. 1 c). It can be interpreted that the porous GDL is first compressed as fibers break and the bulk material becomes denser. As the force increases further, the compressed material is pressed more into the channels, and more force is required to compress the cell due to the increasing counterforce. The channel intrusion and clamping

pressure seem to correlate linearly in the applied force range, as shown in Fig. 1 d). The linear fit ($R^2 > 0.99$) reveals a slope of approximately 61 μm MPa^{-1}, which may assist future analyses in understanding channel intrusion in relation to the applied clamping pressure.

It should be noted that these measurements were carried out at room temperature and dry conditions. The properties of the components may differ during electrochemical characterization.

The results of the electrochemical measurements of compression variation are presented in Fig. 2. The polarization curve and the HFR-free polarization curve (dashed lines at the bottom) are shown in Fig. 2 a). The best cell performance was achieved at 10 %, 20 %, and 40 % compression, with only marginal differences that fall within the measurement reproducibility, see error bars. At 0 % compression, worse performance is observed in the polarization curve. Since the HFR-free curves agree for 0 %–40 % compression, this difference appears to be related solely to ohmic variations, most likely due to insufficient contact between the layers. At 60 % compression, a significantly higher ohmic
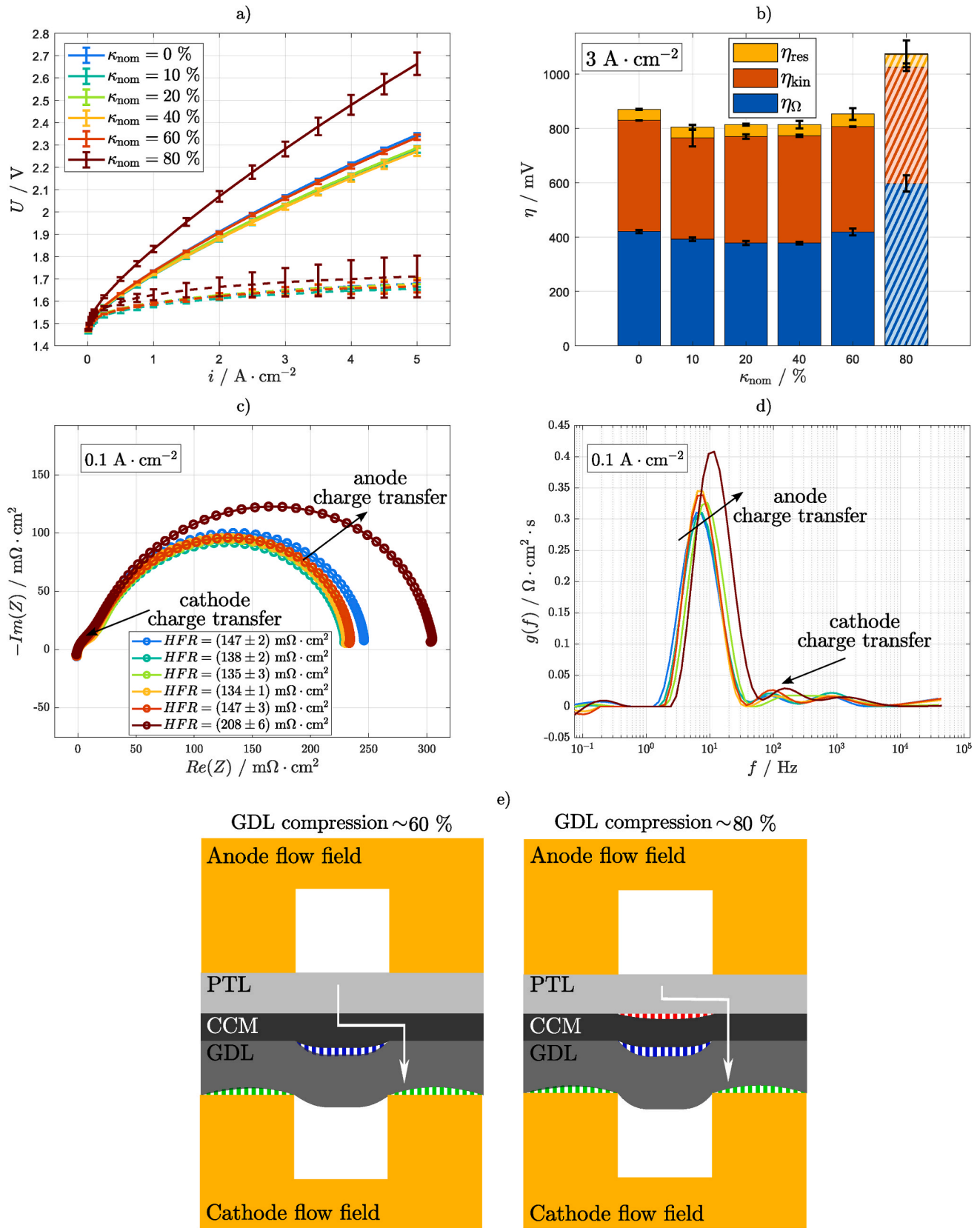
Fig. 2. Electrochemical analysis of different compression of the GDL. a) Polarization curve and HFR-free polarization curve (dashed lines), b) deconvolution of the overpotentials at 3 A cm^{-2}, c) HFR-free EIS at 0.1 A cm^{-2} and d) schematic diagram of the influence of compression on interfacial contacting. The measurements are done at 60 °C, ambient pressure and 150 ml min^{-1} anode water flow.

resistance, but comparable cell polarization, is detected. At 80 % compression, a substantial increase in ohmic overpotential is observed, and the HFR-free polarization curve shows increased values. As discussed above, the GDL at 80 % compression was significantly damaged; therefore, the reproducibility of the measurement is low, see error bars.

Fig. 2 b) shows the voltage breakdown and the contributions of ohmic, kinetic, and residual overpotentials at 3 A cm^{-2} for different compressions. The shaded area for 80 % compression highlights its low reliability due to broken GDL fibers. The ohmic overpotentials reach their minima at 20 % and 40 % compression, with 10 % compression being only slightly higher. Insufficient compression at 0 % and excessive compression at 60 % and 80 % are indicated by significantly higher ohmic overpotentials. The kinetic overpotentials between 10 % and 60 % compression differ by less than 1.5 % from each other, with no observable trend. At 0 % compression, an increase in kinetic overpotentials of approximately 4.4 % compared to the 20 % compression baseline for this study is detected. We attribute this to a loss of active area, as some interfacial contacts are not fully closed, which may be related to the anode and cathode. At 80 % compression, the kinetic overpotentials increase by over 9 % compared to 20 % compression.

The increased kinetic losses are also observable in the impedance spectra and the DRT analysis in Fig. 2 c) and d). We present the impedance at 0.1 A cm^{-2}, where charge transfer resistances are typically dominant. A first peak is detectable in the DRT at around 1 kHz, which we attribute to catalyst layer resistance, appearing insignificant compared to the other processes. At frequencies around 100 Hz, a small capacitive loop is evident, with all spectra being consistent. We associate this loop with the cathode charge transfer process; see the discussion in Fig. 7 regarding low cathode loading CCMs. For 10 %–60 % compression, the spectra across the total frequency range agree with each other, indicating no significant difference in polarization resistance. The 0 % compression shows slightly higher resistance, while 80 % compression exhibits a much higher expansion of the second capacitive loop, usually associated with anode charge transfer. The DRT peak at around 10 Hz confirms that the compression between 0 % and 60 % shows similar polarization, which is significantly increased for 80 % compression. Mass transport resistances do not seem to be affected by compression variation. This may be explained by the fact that the diffusive transport of hydrogen is not a bottleneck in PEM water electrolysis cells, as demonstrated in our previous work, where we purposely blocked pathways in the PTL at the anode and cathode [38]. Furthermore, ionic and electronic in-plane resistivity does not appear to be affected. Low loading CCMs with comparatively low catalyst layer in-plane conductivity may be more sensitive to such compression variations.

Fig. 2 e) illustrates our interpretation of the interfacial contacts under excessive compression of the cell. Increased ohmic resistance can occur due to the bending of the GDL into the flow field channels and the bending of the GDL over the flow field lands (see the dashed areas in white and green over the flow field lands labeled 'GDL compression ∼ 60 %', left). We believe that this phenomenon can occur even under low over-compression and is highly dependent on the cell components used and their stiffness. As the compression increases, the interfacial contact between the GDL and CCM may decrease (see the dashed area in white and blue). Over the flow field channels, the GDL detaches from the CCM, which can only be partially compensated by the flexibility and swelling of the CCM. If the detachment becomes too significant, the area at the cathode becomes partly inactive, and protons in the membrane and electrons in the cathode catalyst layer travel from and to the anode in-plane direction toward active sites, as illustrated by the white arrows. At this point, we would expect a further increase in ohmic resistance due to increased path lengths for the protons and the relatively high in-plane resistivity of the catalyst layer. However, we do not believe that there is a significant impact on cathode charge transfer resistance since neighboring active sites at the cathode compensate for the inactive ones without a substantial increase in cathode kinetic overpotentials, which is typical for the hydrogen evolution reaction (HER). This implies a high

and well-distributed catalyst loading at the cathode. With low catalyst loading at the cathode, this compensation may significantly impact the cathode kinetic overpotentials.

This described scenario applies to the 60 % compression in our study. Further increases in compression may lead to detachment of the CCM from the PTL at the anode (see the dashed area in white and red labeled 'GDL compression ∼ 80 %', right) since the CCM is pressed against the flow field toward the cathode channels, while the titanium PTL remains in place due to its comparatively low flexibility. This detachment may explain the increased charge transfer resistance (see Fig. 2 c)), due to loss of active area at the anode, which cannot be compensated without increased kinetics since the oxygen evolution reaction requires a relatively high amount of activation energy. This scenario may describe cell behavior at 80 % compression.

3.2. GDL contact resistance to coated and uncoated flow field

To analyze the importance of flow field coating, we examined cell bodies with gold coating and without any coating at the anode and cathode separately. The default cell body consists of titanium grade 2, which is coated with 10 μm of gold by electroplating. Beneath the gold layer, there is a 1 μm thick platinum support layer coated galvanically. This coating is commercially available from Umicore AG & Co. KG, Germany.

For comparison, we used a titanium grade 2 cell body that had been used several times in previous electrochemical measurements. The flow field lands showed significant bluish discoloration, which we attribute to a titanium oxide layer of several tens of nanometers. Photos of the coated and uncoated cell bodies are provided in the Supplementary Information SI 4.

Using these cell bodies, we conducted the electrochemical characterization mentioned in the experimental section with a baseline compression of 20 %. Measurements were performed with only the anode flow field coated, only the cathode flow field coated, both flow fields coated, and both flow fields uncoated, see Fig. 3. Fig. 3 a) shows the polarization curves and the HFR-free polarization curves (dashed lines at the bottom) for all combinations. The measured HFR during the polarization curve is presented in Fig. 3 b).

As expected, the case of both flow fields coated shows the best performance and the lowest HFR. Interestingly, with an uncoated anode flow field but a coated cathode flow field, very similar performance and HFR are observed. In contrast, when only the anode flow field is coated, a significant increase in HFR and poor performance is noted. As anticipated, the flow field without any coating demonstrates the worst performance. The HFR-free polarization curve, HFR-free impedance spectra, and DRT analysis at 1 A cm^{-2}, see Fig. 3 c) and d), show that the polarization resistance is not affected by the flow field coating, as expected. The differences in the DRT peaks at approximately 200 mHz are not considered significant and are attributed to measurement reproducibility.

In the case of uncoated flow fields, the titanium-based PTL fibers (20 μm fiber diameter) may penetrate through the titanium oxide layer, circumventing the low electrical resistance and directly contacting the comparably conductive pure titanium. This may be accompanied by "micro-movements" due to temperature and gas pressure effects, which partially remove the oxide layer. Therefore, the ohmic resistance is comparable to that in the case of both flow fields being coated. The still slightly increased HFR may be explained by a much smaller Ti/Ti contact area compared to the softer gold layer.

In the case of the uncoated cathode flow field, the relatively soft and brittle carbon-based fibers cannot penetrate through the titanium oxide layer and only contact its surface, resulting in a high ohmic resistance. It is to be mentioned that the used PTLs may not be perfectly coated with platinum, and some fibers or spots may remain uncoated. Consequently, some titanium fibers might be oxidized to titanium oxide, which increases contact resistance and could potentially falsify the results
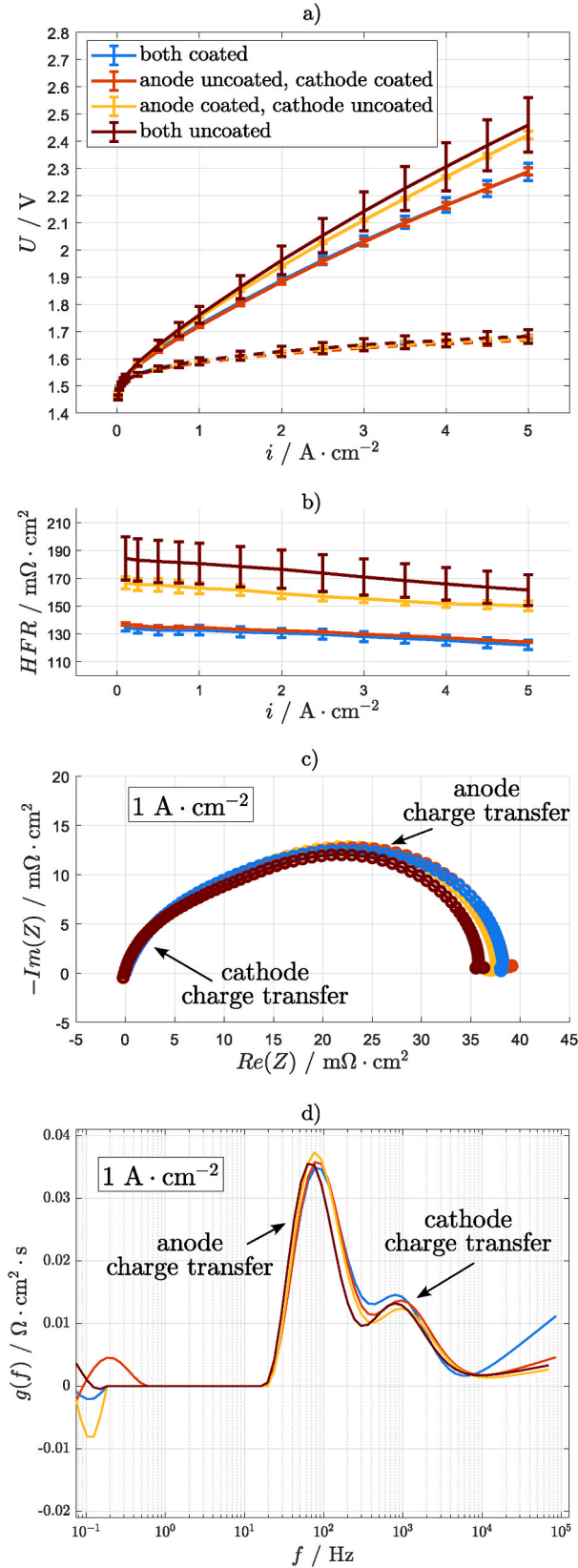
Fig. 3. Electrochemical analysis of the variation of the coating of the flow field. a) Polarization curve, HFR-free polarization curve (dashed lines), b) HFR against current density, c) HFR-free EIS and d) DRT analysis at 1 A cm^{-2}. The measurements are done at 60 °C, ambient pressure and 150 ml min^{-1} anode water flow.

discussed here.

With this study, we demonstrate that a proper electrical interface to carbon-based GDLs is essential to obtain high cell performance. For industrial designs, such as. Using milled flow fields or flow field replacement material like perforated or expanded metals, a highly conductive surface with minimal corrosion effects appears necessary. Our short-term tests reveal that the anode PTL circumvents oxide layers. It should be noted that the durability of the cell, particulary at the interface of uncoated flow field and PTLs, is not investigated here and higher increase of the ohmic resistance over time compared to coated flow fields at the anode is expected.

3.3. Modification of baseline GDL

The produced GDLs with MPLs and PTFE additives were analyzed using CLSM. Fig. 4 shows the CLSM scans of the GDL with and without MPL provided by UCM. The baseline GDL is shown at the top, while the bottom-left panel provides a top view of the MPL. The MPL top view reveals a significant reduction in pore size compared to the GDL without MPL. This reduction in pore size leads to an increased surface area, which is expected to provide a more intimate contact with the catalyst layer and therefore, reduce contact resistances and improve catalyst utilization. The cross-section displaced in the bottom-right panel highlights the structural difference between the bare GDL and GDL with MPL. As discussed in the PEM fuel cell component section, the MPL layer contains 25 wt% PTFE and 75 % wt% acetylene black. In this study, the sample with MPL but without PTFE impregnation is referred to as "UCM MPL", while the GDL substrate with additional 5 wt% PTFE impregnation and MPL is referred to as "UCM MPL + PTFE".

3.4. PEM fuel cell analysis

This section provides results from PEM fuel cell testing and analysis, as the GDL transport properties and cell performance under dry and wet conditions.

3.5. GDL transport properties

To investigate the effects of PTFE and MPL on transport properties, limiting current experiments were performed under both dry and wet operating conditions. Detail limiting current method and testing protocols can be found in the literature [49]. Dry limiting current tests were conducted at 80 °C, 64 % RH, and pressures ranging from 100 to 300 kPa to characterize the oxygen transport properties of the GDL in the absence of liquid water. As shown in Fig. 5 a), the dry oxygen transport resistance for both GDL samples demonstrated a linear relationship with pressure, confirming the absence of water condensation during the experiments. Diffusion media (DM) represent the entire carbon-based layer including MPL if used.

From these results, the tortuosity-to-porosity ratio (τ/ε) can be derived from the slope of the resistance curve, while the pressure-independent transport resistance (Rothers) was determined from the intercept [49]. The dry transport properties of both GDLs are summarized in Table 2. AvCarb MGL370 has a (τ/ε) ratio of 3.86, which is similar to that of Freudenberg H23C8 ($\tau/\varepsilon = 3.79$) [49]. The UCM sample with PTFE and MPL has a slightly lower (τ/ε) ratio of 3.66 due to lower compression strain [50]. Agreeing with the [49], the UCM sample has a higher Rothers due to the Knudsen diffusion effects associated with the MPL's smaller pore sizes.

Wet limiting current experiments, performed at 70 °C, 80 % RH, and 300 kPa absolute pressure with oxygen mole fractions varying from 1 % to 21 %, further evaluated the role of MPL and PTFE in managing liquid water. As shown in Fig. 5 b), the oxygen transport resistance increases sharply as soon as water condensation occurs for the baseline GDL indicating severe flooding in the GDL. In contrast, the UCM MPL + PTFE sample exhibited three distinct regions: dry plateau (~2.3 s/cm),
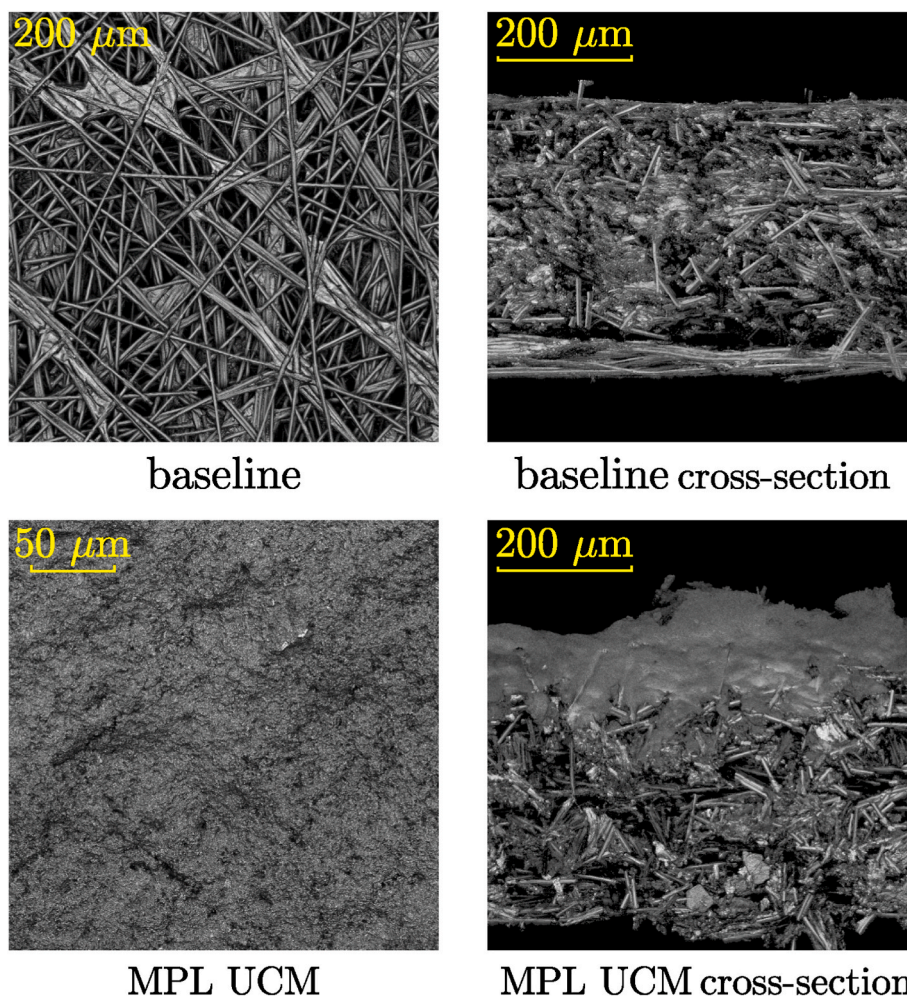
Fig. 4. CLSM scans of the baseline GDL, the baseline GDL with 5 wt% PTFE and top-view and the cross-section of the MPL provided by UCM.

transition, and wet plateau (~4.2 s/cm), highlighting the critical role of MPL and PTFE in mitigating severe GDL and electrode flooding, see Fig. 5 c). The hydrophobic properties and fine pore structure of the MPL effectively prevented water penetration into the catalyst layer, maintaining stable fuel cell performance even at higher current densities. These results emphasize the benefits of MPL and PTFE in enhancing liquid water management in the fuel cell mode.

3.6. PEM fuel cell performance

The fuel cell performance and HFR under both dry and wet conditions are shown in Fig. 6. Under dry conditions, the baseline GDL (bare) and the UCM MPL + PTFE sample exhibit similar performance throughout the entire current density range demonstrating minimal effect from concentration loss. The HFR of the UCM MPL + PTFE is slightly lower than that of the bare GDL likely due to the improvement of the contact resistance between the MPL and the electrode as can be observed from the CLSM images, see Fig. 4. Under wet conditions, the effects of MPL and PTFE impregnation are significant since liquid water management becomes critical. The UCM MPL + PTFE sample demonstrates superior performance, which is consistent with the wet limiting current results shown in Fig. 5 b) and c).

In summary, while the differences under dry conditions are subtle, the UCM MPL + PTFE sample significantly outperforms the baseline GDL under wet conditions. This highlights the critical role of MPL and PTFE impregnation in enhancing water management, reducing HFR, and improving overall fuel cell performance under wet operating conditions.

3.7. PEM water electrolysis analysis

3.7.1. Influence of micro porous layer (MPL) on GDLs

Fig. 7 shows the results of the comparison between *baseline* GDL and GDL *UCM MPL* with employed commercial state-of-the-art CCM and low cathode loading CCM produced at Fraunhofer ISE. The polarization curve in Fig. 7 a) with the commercial CCM shows only slightly improved performance when using the GDL with MPL. The HFR-free curve reveals that beside ohmic, also kinetic and residual overpotentials marginally differ, see also Supplementary Information SI 5. These results indicate the expected positive influence of a MPL. The improved contact and subsequently lowered in plane resistance reduces inactive cell regions and thus also minimizes the activation resistance. The hydrogen diffusion may be as well affected positively as the gas is finely distributed into the GDL. However, we believe due to the high catalyst loading and highly conductive catalyst layer, the commercial CCM does not show huge differences and can be in general used without a MPL on the GDL considering cell performance. However, the cell's durability may be as well positively influenced, but this aspects not discussed in this study.

To analyze the positive influence of a MPL, the results of the measurement with in-house produced CCM with $(0.054 \pm 0.003)\ \mathrm{mg_{Pt} \cdot cm^{-2}}$ cathode catalyst loading are depicted in Fig. 7 b). A remarkable improvement can be seen in both the polarization and HFR-free polarization curves, with high reproducibility, which can be attributed to the
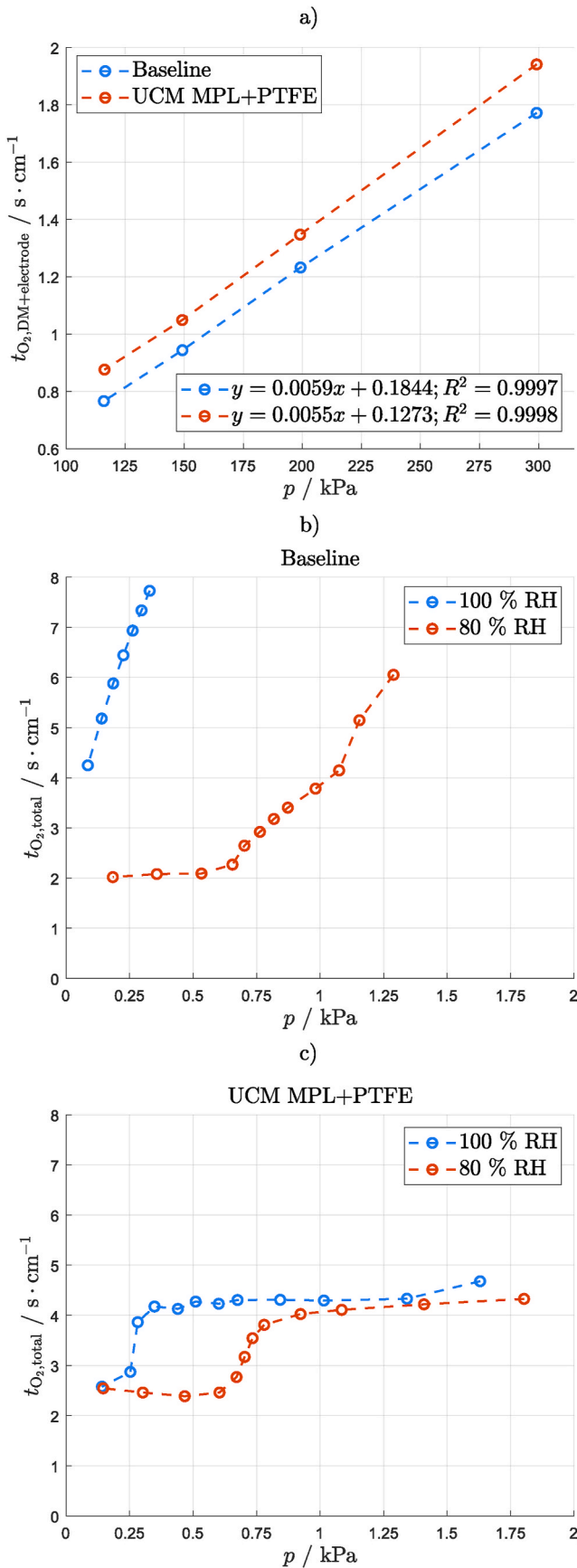
Table 2

Properties of the GDLs under study, subjected to different post-processing steps, as measured by dry limiting current tests conducted at 80°C and 64% RH under a consistent compression strain rate.

Diffusion media	Compressed cathode	Estimated GDL Strain rate (%)	Tortuosity/ Porosity ($\frac{\tau}{\varepsilon}$)	R_{others} (s/m)
	GDL thickness (μm)			
Baseline (bare)	296.4	20	3.86	0.1627
UCM MPL + PTFE	345.8	14	3.65	0.2220

proper coating during the production of the CCM and GDL material. Reduced ohmic (HFR) and kinetic (Tafel slope in the legend of the residual overpotential graphs) resistances are shown in Fig. 7 c) and d). Additionally, the residual overpotentials demonstrate improved behavior at high current densities. At current densities below 2 A cm^{-2}, the residual overpotentials with MPL are increased compared to the baseline, which may be explained by higher capillary pressure due to the smaller pores of the MPL. This effect may become less significant at higher current densities as the produced gas volume increases significantly.

Fig. 7 e) shows the HFR-free EIS and the DRT analysis at 0.1 A cm^{-2} indicating the comparably high cathode charge transfer resistance with the low cathode loading (blue curve). For comparison with the commercial CCM, see Fig. 2 c). With MPL employed, the cathode charge transfer resistance is drastically reduced being comparable with the commercial CCM. As expected, the anode charge transfer resistance seems not to be affected, which is also supported by the consistent DRT peaks.
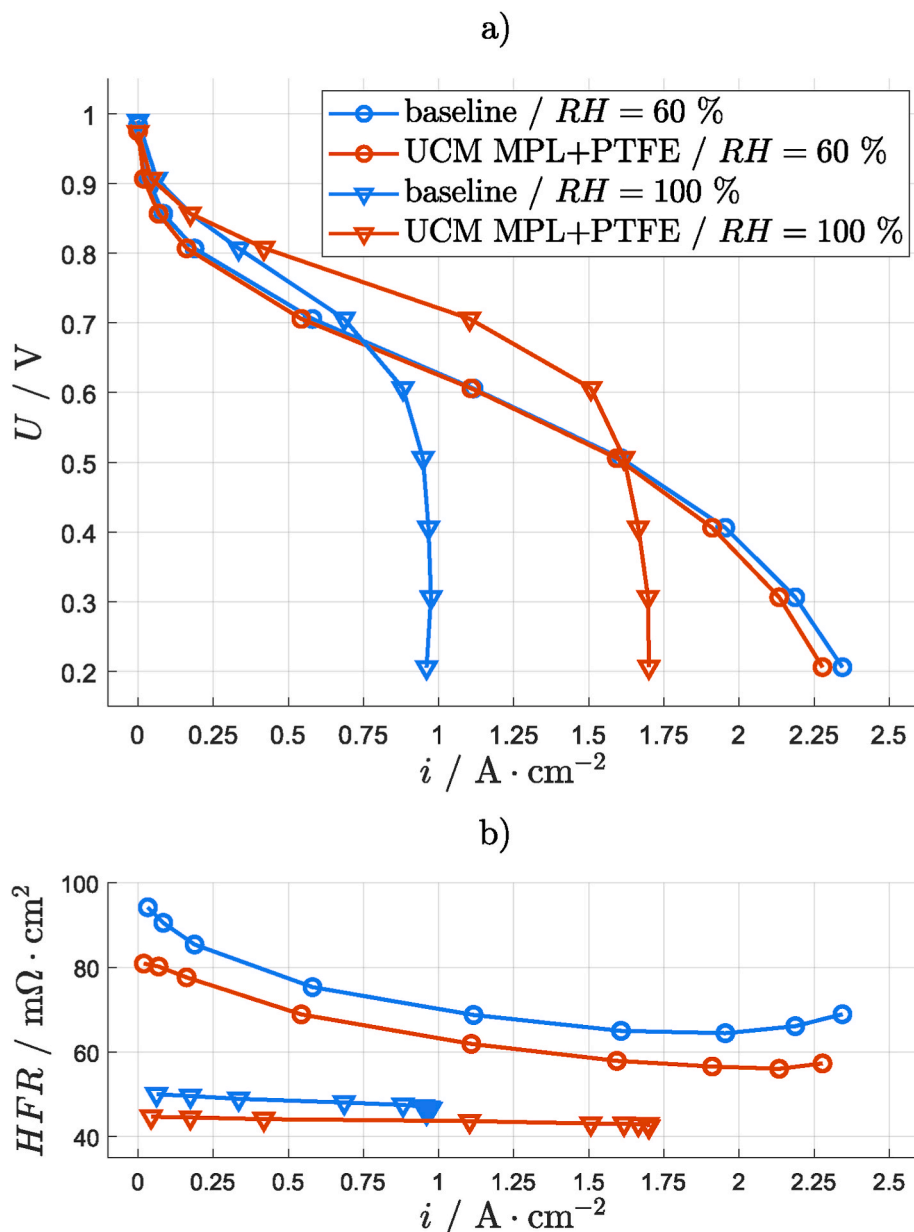
Since the residual overpotentials as well differ significantly, Fig. 7 f) provides the HFR-free EIS and the DRT analysis at 3 A cm^{-2}, revealing reduced polarization resistances with MPL. The charge transfer decreases with current density, and in both cases, additional capacitive and inductive processes at lower frequencies are detected. The inductive loop has been discussed in our previous work and is associated with the membrane or an anode effect [38,39]. In the measurements shown here the differences are not significant and are therefore not discussed. We would associate the capacitive process at ~55 Hz with mass transport resistance at the cathode, as a strong comparison with our previously analysis of blocking PTL pores at the cathode is present, see Ref. [38]. For the impeded cathode mass transport, we did not see an overlapping of the inductive loop, which is very comparable to the measurement shown here. As it seems, these resistances could be minimized by employing the MPL, which may be explained by a better distribution of the evolved gas from the catalyst layer into the GDL.

These findings reveal the impact of optimized interfaces to the catalyst layer when using low-loading CCMs, which is widely discussed for the anode [51–53]. The results clearly demonstrate that the cathode is also of high importance when lowering the overall platinum group metal (PGM) loading of CCMs. Furthermore, the assumption of "non-polarizable" cathode, e.g. for analysis using the Tafel model seems not to be valid at these low cathode loadings.

3.7.2. Hydrophobic treatment (PTFE impregnation) of GDLs

To analyze the influence of hydrophobic treatment the measurements with low-loading CCM and MPL by UCM, with and without 5 wt% PTFE, are shown in Fig. 8. Fig. 8 a) provides the voltage breakdown analysis under default conditions with dry cathode operation and 150 ml min^{-1} at the anode. In Fig. 8 b) both electrodes are flushed with 150 ml min^{-1} water.

During operation with and without water flow at the cathode, no significant difference in cell performance is observed. The HFR analysis over current density reveal increased ohmic resistance with 5 wt% PTFE

Fig. 5. Oxygen transport resistance under a) dry (80 °C, 64 % RH) and wet (70 °C, 80 % RH, 300 kPa ab) operating conditions for b) baseline GDL and c) UCM MPL + PTFE GDL.

a)

b)

Fig. 6. Electrochemical analysis of baseline GDL and GDL treated with MPL and PTFE in PEM fuel cell operation at relative humidity of 60 % and 100 %. a) Polarization curve and b) HFR against current density.

amount which is expected due to the non-conductive properties of PTFE. The HFR-free polarization curves indicate slightly higher overpotentials in both cases with PTFE. The Tafel slope (see legend of residual overpotential graphs) also shows marginally increased values. Since the amount of PTFE of the MPL that contacts the catalyst layer is not affected by the PTFE amount of the GDL, this dependency is not clear at this point. When applying water to the cathode no significant differences to operation with dry cathode are detected in the polarization curve, see Fig. 8 b). Again, the same trend is observed, as the sample with PTFE shows slightly lower performance, primarily attributed to the increased HFR, as indicated by the HFR-free polarization curve and the HFR over current density.

When comparing Fig. 8 a) and b), the HFR decreases when applying water to the cathode the decrease is less pronounced with increasing current density. We attribute this to better thermal management of the cell due to the higher heat capacity of the cathode water, which is especially relevant at low current densities and with less reaction heat. This improved thermal management decreases the membrane resistance

and helps maintain a more stable temperature as the reaction heat increases with current density.

The Tafel slope does not show significant differences between dry cathode and both electrodes supplied with water, which is atypical due to the differences in temperature as the applied water may remove produced heat of the HER. Since the water applied to the cathode mostly affects the cathode itself, this effect may be negligible due to the overall small overpotentials of the HER. The residual overpotentials show clearly increased values with water supply to the cathode, exceeding 70 mV at 5 A cm^{-2} for the sample with and without PTFE. This increase may be attributed to enhanced cathode mass transport for water-flooded cathode catalyst layers, as described by Bernt et al. [54]. They describe cathode mass transport related overpotentials up to 24 mV at 3 A cm^{-2} under dry cathode operation, considering electro-osmotic drag of ~3 water molecules per proton. At 3 A cm^{-2}, we observe a difference of ~40 mV between dry cathode and water flushed cathode operation. The application of water to the cathode may significantly increase capillary pressure within the catalyst and gas diffusion layer, leading to
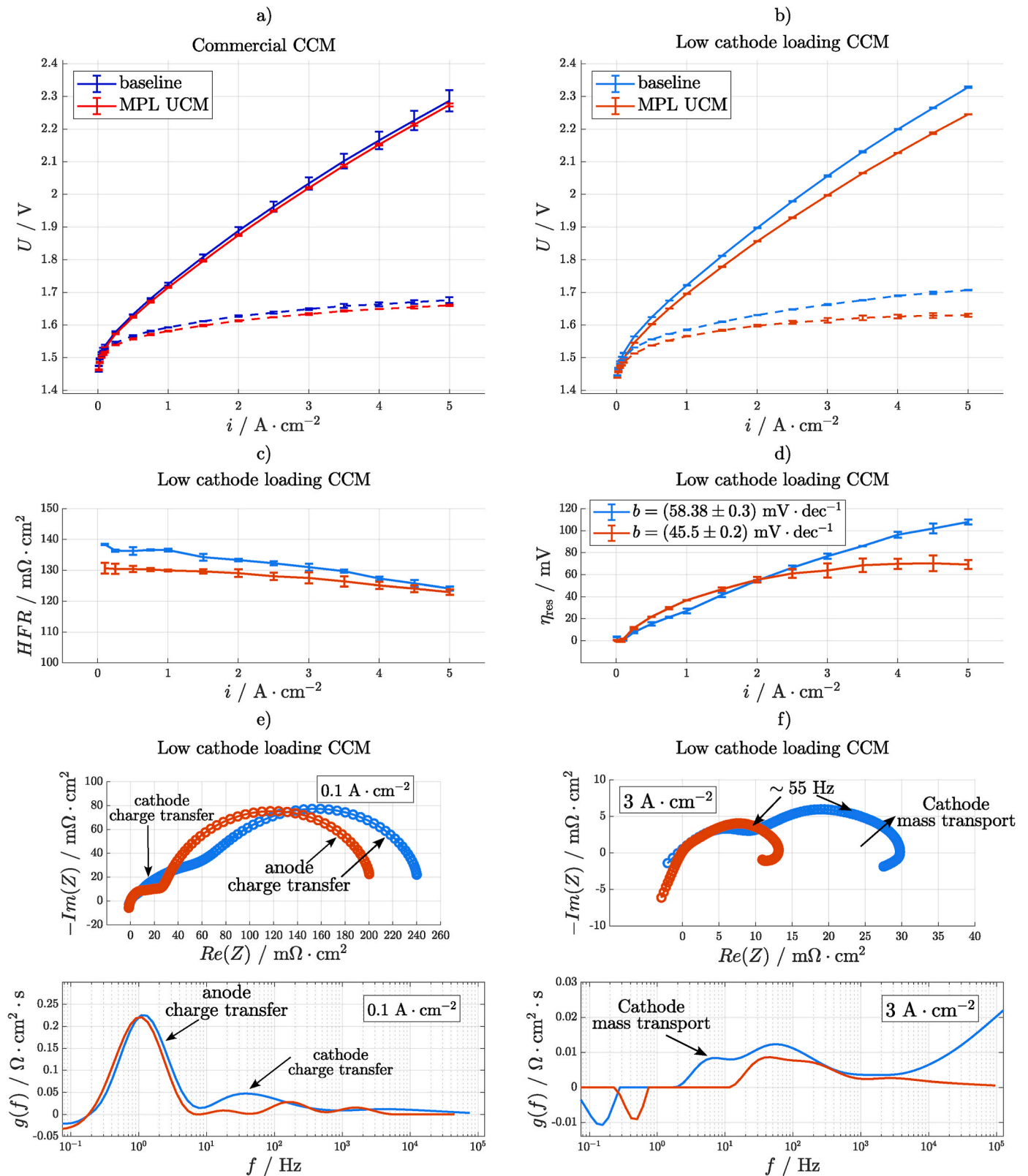
Fig. 7. Electrochemical analysis of the influence of a MPL on top of the GDL at the cathode compared with the baseline GDL material. Polarization curve and HFR-free polarization curve (dashed lines) with a) commercial CCM and b) low cathode loading CCM, c) HFR and d) residual overpotentials over current density with Tafel slope depicted in the legend and e) EIS analysis in Nyquist (top) and DRT (bottom) presentation at 0.1 A cm^{-2} and f) at 3 A cm^{-2} with the low loading CCM employed. The measurements are done at 60 °C, ambient pressure and 150 ml min^{-1} anode water flow.
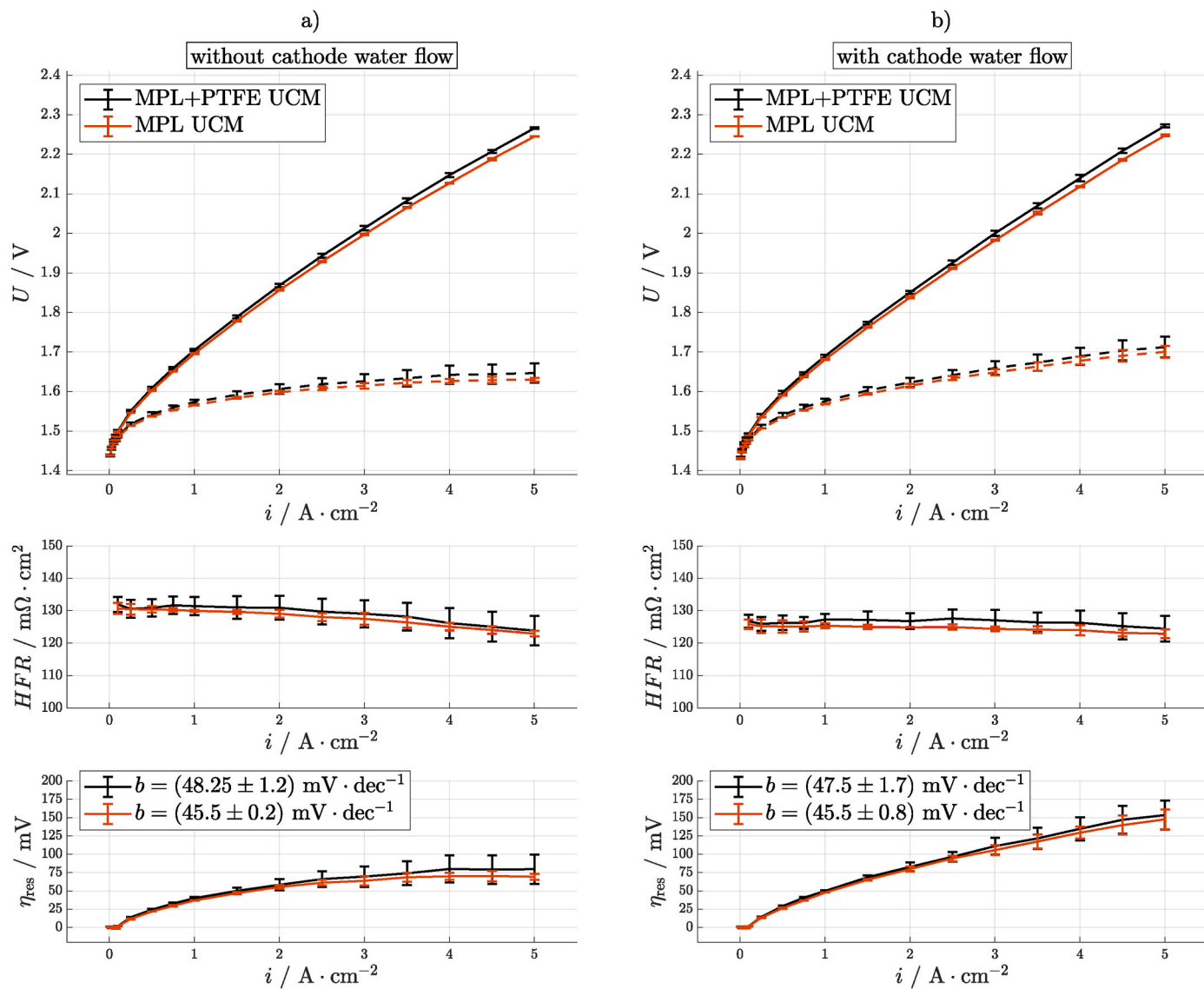
Fig. 8. Electrochemical analysis of the influence of hydrophobic treatment (PTFE) in the GDL at the cathode using the low-loading CCM and comparing MPL UCM and MPL + PTFE UCM. Polarization curve, HFR-free polarization curve (dashed lines), HFR and residual overpotentials over current density at a) dry cathode and b) with water flow at the cathode. The measurements are done at 60 °C, ambient pressure and 150 ml min^{-1} anode water flow.

extraordinary increases in hydrogen mass transport losses. Additionally, a reduction in the electronic in-plane conductivity of the cathode catalyst layer may also be plausible. The measurements with commercial CCM are similarly analyzed and presented in the Supplementary Information SI 6 but do not reveal different trends compared to those shown for the low-loading CCM.

4. Conclusion

This work analyzes the usage of carbon-based PTLs and MPLs at the cathode within PEM water electrolysis cells concerning cell performance. The influence of cell compression, contact with coated and uncoated titanium flow fields, the use of a microporous layer, and hydrophobic additives are investigated using a state-of-the-art cell setup.

We show that cell compression sensitively effects the overall contact resistance determined by high frequency resistance measurements. Insufficient compression can occur below 10 % and excessive compression above 60 % GDL compression for the GDL material used in this study. At a cell compression of ~80 %, an increasing charge transfer

resistance was observed at the anode, measured by impedance spectroscopy. Using a confocal laser scanning microscope, the GDL compression was analyzed after electrochemical in situ measurements. Visualization of ex situ compression analysis provides insights into the mechanical behavior of the GDL and the cell at different compressions. Through these analyses, hypotheses regarding cell mechanics, internal contact resistance, and detachment of the CCM from the GDL at the cathode, as well as from the PTL at the anode, are proposed.

Measurements employing gold-coated and uncoated titanium flow fields at anode and cathode shows a significant impact on the contact resistance at the cathode and comparatively less impact at the anode. These phenomena are explained by the titanium fibers of an anode PTL, which penetrate the titanium oxide layer due to their hardness. The comparable soft carbon fibers appear not to be able to penetrate this oxide layer. As intended, no impact on cell polarization could be seen.

The impact of carbon-based micro porous layer on top of the GDL is evaluated in a standard cell setup with a commercial CCM with state-of-the-art loading and a purpose-made CCM produced at Fraunhofer ISE with low cathode loading of ⟨ 0.06 mg$_{Pt}$·cm^{-2}. As expected, the commercial CCM demonstrated only slight improvements with the addition

of an MPL. The comparatively high state-of-the-art platinum loading, accompanied by a high carbon loading, minimizes the in-plane resistance of the catalyst layer.

In contrast, using the CCM with low cathode catalyst loading, the MPL provides a significant improvement in ohmic, kinetic, and residual overpotentials. The impedance spectra show a significant reduction in both cathode charge transfer and mass transport resistance, which we attribute to improved contact and reduced inactive catalyst layer surface area.

The influence of PTFE additives was analyzed applying an impregnation of ~5 wt% PTFE in the GDL with MPL and for the case of a CCM with a low cathode loading. Increased ohmic resistance is measured for an impregnated GDL, which is referred to the non-conductive properties of PTFE. When applying a water flow to the cathode, increased residual overpotentials are measured for both GDLs (with and without PTFE) which may be explained by increased hydrogen transport resistivity due to the water-flooded catalyst layer at the cathode.

This study demonstrates that a simple transfer of PEM fuel cell materials, such as GDLs with PTFE, does not necessarily justify the associated production efforts or guarantee a positive impact on cell performance. The use of MPLs is highly recommended when employing low catalyst loadings at the cathode; however, the addition of 5 wt% PTFE impregnation did not show an improvement in terms of cell performance. Furthermore, proper electrical contact and compression of carbon-based GDLs are essential for optimal cell performance. Since this work focuses solely on cell performance, further measurements and electrochemical modeling regarding cell durability are suggested.

CRediT authorship contribution statement

Niklas Hensle: Writing – original draft, Visualization, Validation, Project administration, Methodology, Investigation, Data curation, Conceptualization. **Justin Hoffmann:** Visualization, Methodology,

Investigation, Data curation. **Zabihollah Najafianashrafi:** Investigation, Data curation. **Tom Smolinka:** Writing – review & editing, Supervision, Funding acquisition, Conceptualization. **Po-Ya Abel Chuang:** Writing – review & editing, Supervision, Conceptualization. **André Weber:** Writing – review & editing, Supervision, Funding acquisition, Conceptualization.

Declaration of generative AI and AI-assisted technologies in the writing process

During the preparation of this work the authors used a Fraunhofer internal version of ChatGPT 4o Mini in order to improve language and readability. After using this tool/service, the authors reviewed and edited the content as needed and take full responsibility for the content of the publication.

Declaration of competing interest

The authors declare that they have no known competing financial interests or personal relationships that could have appeared to influence the work reported in this paper.

Acknowledgment

List of abbreviations

GDL	Gas diffusion layer
EIS	Electrochemical impedance spectroscopy
DRT	Distribution of relaxation time
PTL	Porous transport layer
PEMFC	Proton exchange membrane fuel cell
MPL	Micro porous layer
HFR	High frequency resistance
CLSM	confocal laser scanning microscopy
CCM	Catalyst-coated membrane
PTFE	Polytetrafluoroethylene
PEEK	polyether ether ketone
Nom	Nominal
Hs	Hard stop
Ω	Ohmic
Kin	Kinetic
Res	residual
NLPM	Norm liter per minute
HER	Hydrogen evolution reaction
DM	Diffusion media

Appendix A. Supplementary data

Supplementary data to this article can be found online at https://doi.org/10.1016/j.jpowsour.2025.236913.

Data availability

Data will be made available on request.

References

[1] Montaño DL. Canelas, P. Ruiz García, A. Jerez Navarro, M. Aguirre Gomez, J. J. López Cascales, Effect of the cathodic gas diffusion layer on the performance of a

proton exchange membrane electrolyzer, Energies 17 (21) (2024) 5298, https://doi.org/10.3390/en17215298.

[2] J. Hemauer, S. Rehfeldt, H. Klein, A. Peschel, Performance and cost modelling taking into account the uncertainties and sensitivities of current and next-generation PEM water electrolysis technology, Int. J. Hydrogen Energy 48 (66) (2023) 25619–25634.

[3] X.-Z. Yuan, N. Shaigan, C. Song, M. Aujla, V. Neburchilov, J.T.H. Kwan, D. P. Wilkinson, A. Bazylak, K. Fatih, The porous transport layer in proton exchange membrane water electrolysis: perspectives on a complex component, Sustain. Energy Fuels 6 (8) (2022) 1824–1853, https://doi.org/10.1039/D2SE00260D.

[4] J.C. Cruz, R. Barbosa, B. Escobar, Z. Zarhri, D.L. Trejo-Arroyo, B. Pamplona, L. Gómez-Barba, Electrochemical and microstructural analysis of a modified gas diffusion layer for a PEM water electrolyzer, Int. J. Electrochem. Sci. 15 (6) (2020) 5571–5584.

[5] F. Madadi, A. Rezaeian, H. Edris, M. Zhiani, Improving performance in PEMFC by applying different coatings to metallic bipolar plates, Mater. Chem. Phys. 238 (2019) 121911.

[6] T. Wilberforce, O. Ijaodola, E. Ogungbemi, F.N. Khatib, T. Leslie, Z. El-Hassan, J. Thompson, A.G. Olabi, Technical evaluation of proton exchange membrane (PEM) fuel cell performance – a review of the effects of bipolar plates coating, Renew. Sustain. Energy Rev. 113 (2019) 109286.

[7] J. Ge, A. Higier, H. Liu, Effect of gas diffusion layer compression on PEM fuel cell performance, J. Power Sources 159 (2) (2006) 922–927.

[8] A.H. Mahmoudi, A. Ramiar, Q. Esmaili, Effect of inhomogeneous compression of gas diffusion layer on the performance of PEMFC with interdigitated flow field, Energy Convers. Manag. 110 (2016) 78–89.

[9] Q. Shi, C. Feng, P. Ming, F. Tang, C. Zhang, Compressive stress and its impact on the gas diffusion layer: a review, Int. J. Hydrogen Energy 47 (6) (2022) 3994–4009.

[10] H.-M. Chang, C.-W. Lin, M.-H. Chang, H.-R. Shiu, W.-C. Chang, F.-H. Tsau, Optimization of polytetrafluoroethylene content in cathode gas diffusion layer by the evaluation of compression effect on the performance of a proton exchange membrane fuel cell, J. Power Sources 196 (8) (2011) 3773–3780.

[11] M. Sarker, M.A. Rahman, F. Mojica, S. Mehrazi, W.J. Kort-Kamp, P.-Y.A. Chuang, Experimental and computational study of the microporous layer and hydrophobic treatment in the gas diffusion layer of a proton exchange membrane fuel cell, J. Power Sources 509 (2021) 230350, https://doi.org/10.1016/j.jpowsour.2021.230350.

[12] S. Mehrazi, M. Sarker, P.-Y.A. Chuang, Effect of high aspect ratio additives on microstructural and mass transport properties of the microporous layer in a proton exchange membrane fuel cell, J. Power Sources 580 (2023) 233361.

[13] S. Park, J.-W. Lee, B.N. Popov, A review of gas diffusion layer in PEM fuel cells: materials and designs, Int. J. Hydrogen Energy 37 (7) (2012) 5850–5865.

[14] N. Hensle, S. Metz, A. Weber, T. Smolinka, A segmented along the channel test cell for locally resolved analysis at high current densities in PEM water electrolysis, J. Electrochem. Soc. (2024), https://doi.org/10.1149/1945-7111/ad9064.

[15] M. Suermann, T. Gimpel, L.V. Bühre, W. Schade, B. Bensmann, R. Hanke-Rauschenbach, Femtosecond laser-induced surface structuring of the porous transport layers in proton exchange membrane water electrolysis, J. Mater. Chem. A 8 (9) (2020) 4898–4910, https://doi.org/10.1039/C9TA12127G.

[16] M. Mandal, M. Secanell, Improved polymer electrolyte membrane water electrolyzer performance by using carbon black as a pore former in the anode catalyst layer, J. Power Sources 541 (2022) 231629.

[17] P.J. Kim, C. Lee, J.K. Lee, K.F. Fahy, A. Bazylak, In-plane transport in water electrolyzer porous transport layers with through pores, J. Electrochem. Soc. 167 (12) (2020) 124522, https://doi.org/10.1149/1945-7111/abb173.

[18] H. Janßen, S. Holtwerth, W. Zwaygardt, A. Stähler, W. Behr, D. Federmann, M. Carmo, W. Lehnert, M. Müller, A facile and economical approach to fabricate a single-piece bipolar plate for PEM electrolyzers, Int. J. Hydrogen Energy 49 (2024) 816–828.

[19] Z. Fan, H. Yu, G. Jiang, D. Yao, S. Sun, J. Chi, B. Qin, Z. Shao, Low precious metal loading porous transport layer coating and anode catalyst layer for proton exchange membrane water electrolysis, Int. J. Hydrogen Energy 47 (44) (2022) 18963–18971.

[20] M. Cieluch, D. Düerkop, N. Kazamer, F. Wirkert, P. Podleschny, U. Rost, A. Schmiemann, M. Brodmann, Manufacturing and investigation of MEAs for PEMWE based on glass fibre reinforced PFSA/ssPS composite membranes and catalyst-coated substrates prepared via catalyst electrodeposition, Int. J. Hydrogen Energy 52 (2024) 521–533.

[21] L.V. Bühre, S. Bullerdiek, P. Trinke, B. Bensmann, A.-L.E.R. Deutsch, P. Behrens, R. Hanke-Rauschenbach, Application and analysis of a salt bridge reference electrode setup for PEM water electrolysis: towards an extended voltage loss break down, J. Electrochem. Soc. 169 (12) (2022) 124513, https://doi.org/10.1149/1945-7111/ac9ee1.

[22] Ortiz E. Cruz, N. van Treel, S. Koch, S. Vierrath, M. Bühler, The effect of compression on PEM Electrolyzer membrane electrode Assemblies, J. Power Sources 614 (2024) 235018.

[23] M. Stähler, A. Stähler, F. Scheepers, M. Carmo, W. Lehnert, D. Stolten, Impact of porous transport layer compression on hydrogen permeation in PEM water electrolysis, Int. J. Hydrogen Energy 45 (7) (2020) 4008–4014.

[24] A. Martin, P. Trinke, M. Stähler, A. Stähler, F. Scheepers, B. Bensmann, M. Carmo, W. Lehnert, R. Hanke-Rauschenbach, The effect of cell compression and cathode pressure on hydrogen crossover in PEM water electrolysis, J. Electrochem. Soc. 169 (1) (2022) 14502, https://doi.org/10.1149/1945-7111/ac4459.

[25] Z. Kang, S.M. Alia, J.L. Young, G. Bender, Effects of various parameters of different porous transport layers in proton exchange membrane water electrolysis,

Electrochim. Acta 354 (2020) 136641, https://doi.org/10.1016/j.electacta.2020.136641.

[26] Lickert T, Fischer S, Young JL, Klose S, Franzetti I, Hahn D, Kang Z, Shviro M, Scheepers F, Carmo M, Smolinka T, Bender G, Metz S. Advances in Benchmarking and Round Robin Testing for PEM Water Electrolysis: Reference Protocol and Hardware. 0306-2619 2023;vol. 352:121898.doi:10.1016/j.apenergy.2023.121898.

[27] T. Kennerknecht, Fatigue of Micro Molded Materials - Aluminum Bronze and Yttria Stabilized Zirconia, KIT Scientific Publishing, 2014.

[28] T. Straub, Experimental Investigation of Crack Initiation in Face-Centered Cubic Materials in the High and Very High Cycle Fatigue Regime, KIT Scientific Publishing, 2016.

[29] S.A. Slaby, O. Kraft, C. Eberl, Fatigue properties of conventionally manufactured and micro-powder-injection-moulded 17-4PH micro-components, Fatig. Fract. Eng. Mater. Struct. 39 (6) (2016) 780–789, https://doi.org/10.1111/ffe.12416.

[30] T. Straub, J. Fell, S. Zabler, T. Gustmann, H. Korn, S.C.L. Fischer, Characterization of filigree additively manufactured NiTi structures using micro tomography and micromechanical testing for metamaterial material models, Materials 16 (2) (2023) 676, https://doi.org/10.3390/ma16020676.

[31] A.-S. Feiner, A.J. McEvoy, The Nernst equation, J. Chem. Educ. 71 (6) (1994) 493.

[32] P.J. Kim, J.K. Lee, C. Lee, K.F. Fahy, P. Shrestha, K. Krause, H.W. Shafaque, A. Bazylak, Tailoring catalyst layer interface with titanium mesh porous transport layers, Electrochim. Acta 233 (2021) 137879.

[33] Pierre Millet, PEM water electrolysis, in: Hydrogen Production, John Wiley & Sons, Ltd, 2015, pp. 63–116.

[34] I. Franzetti, A. Pushkarev, A.-L. Chan, T. Smolinka, Parasitic effects in impedance spectrum of PEM water electrolysis cells: case study of high-frequency inductive effects, Energ. Tech. 11 (12) (2023), https://doi.org/10.1002/ente.202300375.

[35] P. Kurzweil, O. Dietlmeier, Elektrochemische Speicher: Superkondensatoren, Batterien, Elektrolyse-Wasserstoff, Rechtliche Rahmenbedingungen, second ed., Springer Vieweg, Wiesbaden, 2018.

[36] M. Suermann, T.J. Schmidt, F.N. Büchi, Cell performance determining parameters in high pressure water electrolysis, Electrochim. Acta 211 (2016) 989–997.

[37] T. Miličić, H. Altaf, N. Vorhauer-Huget, L.A. Živković, E. Tsotsas, T. Vidaković-Koch, Modeling and analysis of mass transport losses of proton exchange membrane water electrolyzer, Processes 10 (11) (2022) 2417, https://doi.org/10.3390/pr10112417.

[38] D. Brinker, N. Hensle, La Horstmann de Viña, Irene Franzetti, Bühre LV. Jerónimo, U.A. Andaluri, C. Menke, T. Smolinka, A. Weber, Inductive Loops in Impedance Spectra of PEM Water Electrolyzers, 2024.

[39] N. Hensle, D. Brinker, S. Metz, T. Smolinka, A. Weber, On the role of inductive loops at low frequencies in PEM electrolysis, Electrochem. Commun. 155 (2023) 107585.

[40] T. Schuler, T.J. Schmidt, F.N. Büchi, Polymer electrolyte water electrolysis: correlating performance and porous transport layer structure: Part II. Electrochemical performance analysis, J. Electrochem. Soc. 166 (10) (2019) F555–F565, https://doi.org/10.1149/2.1241908jes.

[41] E. Padgett, G. Bender, A. Haug, K. Lewinski, F. Sun, H. Yu, D.A. Cullen, A. J. Steinbach, S.M. Alia, Catalyst layer resistance and utilization in PEM electrolysis, J. Electrochem. Soc. 170 (8) (2023) 84512, https://doi.org/10.1149/1945-7111/acee25.

[42] M. Schönleber, D. Klotz, E. Ivers-Tiffée, A method for improving the robustness of linear kramers-kronig validity tests, Electrochim. Acta 131 (2014) 20–27.

[43] B.A. Boukamp, A linear kronig-kramers transform test for immittance data validation, J. Electrochem. Soc. 142 (6) (1995) 1885–1894, https://doi.org/10.1149/1.2044210.

[44] H. Schichlein, A.C. Müller, M. Voigts, A. Krügel, E. Ivers-Tiffée, Deconvolution of electrochemical impedance spectra for the identification of electrode reaction mechanisms in solid oxide fuel cells, J. Appl. Electrochem. 32 (8) (2002) 875–882, https://doi.org/10.1023/A:1020599525160.

[45] A. Leonide, V. Sonn, A. Weber, E. Ivers-Tiffée, Evaluation and modeling of the cell resistance in anode-supported solid oxide fuel cells, J. Electrochem. Soc. 155 (1) (2008) B36, https://doi.org/10.1149/1.2801372.

[46] E. Ivers-Tiffée, A. Weber, Evaluation of electrochemical impedance spectra by the distribution of relaxation times, J. Ceram. Soc. Japan 125 (4) (2017) 193–201, https://doi.org/10.2109/jcersj2.125.P4-1.

[47] Chan A-L, Yu H, Reeves KS, Alia SM. Identifying Electrochemical Processes by Distribution of Relaxation Times in Proton Exchange Membrane Electrolyzers. 0378-7753 2025;vol. 628:235850.

[48] A. Schiefer, M. Heinzmann, A. Weber, Inductive low-frequency processes in PEMFC-impedance spectra, Fuel Cells (2020), https://doi.org/10.1002/fuce.201900212.

[49] P.-Y.A. Chuang, M.A. Rahman, F. Mojica, D.S. Hussey, D.L. Jacobson, J. M. LaManna, The interactive effect of heat and mass transport on water condensation in the gas diffusion layer of a proton exchange membrane, Fuel Cell 480 (2020) 229121.

[50] H. Zhang, L. Zhu, H.B. Harandi, K. Duan, R. Zeis, P.-C. Sui, P.-Y.A. Chuang, Microstructure reconstruction of the gas diffusion layer and analyses of the anisotropic transport properties, Energy Convers. Manag. 241 (2021) 114293.

[51] S. Siracusano, V. Baglio, N. van Dijk, L. Merlo, A.S. Aricò, Enhanced performance and durability of low catalyst loading PEM water electrolyser based on a short-side chain perfluorosulfonic ionomer, 0306-2619 192 (2017) 477–489.

[52] T. Schuler, C.C. Weber, J.A. Wrubel, L. Gubler, B. Pivovar, F.N. Büchi, G. Bender, Ultrathin microporous transport layers: implications for low catalyst loadings, thin membranes, and high current density operation for proton exchange membrane

electrolysis, Adv. Energy Mater. 14 (7) (2024) 2302786, https://doi.org/10.1002/aenm.202302786.

[53] M. Bernt, A. Siebel, H.A. Gasteiger, Analysis of voltage losses in PEM water electrolyzers with low platinum group metal loadings, J. Electrochem. Soc. 165 (5) (2018) F305–F314.

[54] M. Bernt, H.A. Gasteiger, Influence of ionomer content in IrO 2/TiO 2 electrodes on PEM water electrolyzer performance, J. Electrochem. Soc. 163 (11) (2016) F3179–F3189, https://doi.org/10.1149/2.0231611jes.